# Design of a Carousel Process for Cesium Removal Using Crystalline Silicotitanate

**Benjamin J. Hritzko**
School of Chemical Engineering, Purdue University, West Lafayette, IN 47907

**D. Douglas Walker**
Westinghouse Savannah River Company, Aiken, SC 29808

**N.-H. Linda Wang**
School of Chemical Engineering, Purdue University, West Lafayette, IN 47907

*A three-column carousel process based on a pelletized form of CST powder was designed to remove radioactive $^{137}Cs^+$ from SRS nuclear wastes. A multicomponent ion-exchange equilibrium model was used to generate cesium loading data, which were fit to the Langmuir equation to obtain effective single-component cesium isotherm parameters for representative wastes. Mass-transfer parameters were estimated by analyzing breakthrough curves for two simulated wastes. Simulations based on a pore-diffusion rate model were performed to determine the lengths of the mass-transfer zone for different feed compositions and linear velocities. The length of a single segment in the carousel process was the constant-pattern mass-transfer zone to ensure consistent high column utilization during startup and cyclic steady state. Analysis of the dimensionless groups in the mass balance equations revealed that the mass-transfer zone length is proportional to the particle Peclet number. The proportionality constant is a function of the waste composition and the $Cs^+$ concentration in the waste. A higher distribution coefficient and isotherm nonlinearity result in a smaller proportionality constant. With this analysis designs can be easily adjusted for variations in isotherms, feed concentration, particle size, linear velocity, and intraparticle diffusivity.*

## Introduction

Over 100 million gallons of radioactive waste, generated by nuclear reactors and weapon production plants, is now in underground storage tanks at Dept. of Energy sites in Hanford, Savannah River, Oak Ridge, Idaho, and Fernald (McGinnis et al., 1995). The cost for treating this waste using current technologies is estimated at 100 billion dollars (McGinnis et al., 1995). After the initial treatment, the waste in its final form is proposed to be vitrified in borosilicate glass for permanent storage.

Several different approaches are currently under investigation for treating the supernatant before it is placed in long-term storage (McGinnis et al., 1995). The present study is focused on crystalline Silicotitanate (CST) ion exchange for treatment of Savannah River Site (SRS) wastes. CST has a high affinity for the major radioactive contaminant $^{137}Cs^+$. Because the affinity is high, a large amount of $^{137}Cs^+$ can be confined within a small volume of saturated CST particles. The cost of making glass canisters is expected to be quite high, so it is important to utilize the CST exchanger as much as possible. A continuous carousel process with three packed columns in series is proposed (Figure 1). In step $N$ of this design the lead column (A) is saturated, the second column (B) contains the mass-transfer zone, and the third column (C) is a guard column. When the lead column is saturated, it is taken off-line at step $N+1$ for permanent storage and the feed is introduced to what was previously the second column (B) in the series. A fresh column (D) is introduced to the end of the train and acts as the new buffer column. Another new

Correspondence concerning this article should be addressed to N.-H. L. Wang.

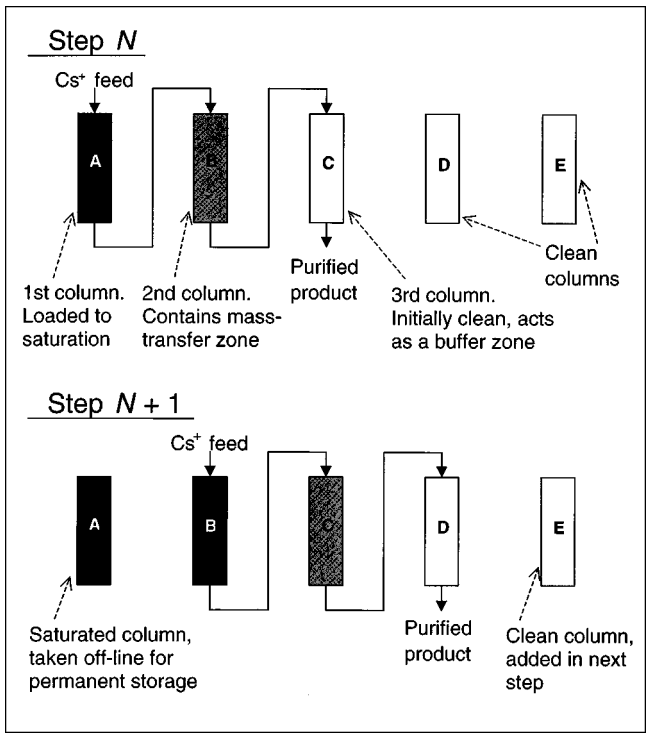


**Figure 1. Proposed carousel process.**

column (E) can be added to the end of the series in step $N+2$. The carousel design allows the cesium level in the decontaminated waste to be below the required levels (less than $1.3\times10^{-6}$ kg/m$^3$ $Cs^+$) and allows almost full utilization of the adsorbent (Ernest et al., 1997).

The CST ion exchanger in a powder form was developed at Texas A&M University and Sandia National Laboratory (Anthony et al., 1993, 1994). UOP later produced CST pellets by mixing the CST powder with a binder. This binder makes the CST feasible for column applications, but it is expected to give the pellets a slightly lower effective capacity per unit weight than the powder (McCabe, 1995, 1997). Prior to the pelletized product IONSIV IE-911, UOP made a pre-production lot (IE-910 07398-38B), which was tested by DOE labs. Subsequently, UOP offered IONSIV IE-911 for commercial use. Several lots have been produced, sold, and tested.

Zheng et al. (1997) developed a detailed multicomponent ion-exchange model, the ZAME (Zheng, Anthony, Miller equilibrium) model, that described the uptake of $Cs^+$ on CST powder in the presence of competing ions. They validated the model by comparing its predictions to batch experimental data. Equilibrium uptake of $Cs^+$ on CST powder in the multicomponent SRS wastes is a complex function of the concentration of each component in the mixture. The model takes multicomponent competitive ion exchange into account. In this work, the uptake of $Cs^+$ predicted by the ZAME model is correlated to an effective single-component Langmuir isotherm for six representative SRS waste compositions (Table 1). The batch test data obtained for CST pellets can be explained by using the ZAME model predictions (for CST powder) multiplied by a dilution factor of 0.56 to 1.0, depending on the waste composition, the lot of pellets, and the

**Table 1. SRS Waste Simulant Compositions**

| | Concentration (kmol/m$^3$) | | | | | |
|---|---|---|---|---|---|---|
| Component | Avg. | Avg.* | High $OH^-$ | High $OH^-$* | High $NO_3^-$ | High $NO_3^-$* |
| $Na^+$ | 5.6 | 5.47 | 5.6 | 5.48 | 5.6 | 5.45 |
| $K^+$ | 0.015 | 0.15 | 0.03 | 0.15 | 0.0041 | 0.15 |
| $Cs^+$ | 0.00014 | 0.0007 | 0.00037 | 0.0007 | 0.00014 | 0.0007 |
| $AlO_2^-$ | 0.31 | 0.31 | 0.27 | 0.27 | 0.32 | 0.32 |
| $C_2O_4^-$ | 0.008 | 0.008 | 0.008 | 0.008 | 0.008 | 0.008 |
| $CO_3^{2-}$ | 0.16 | 0.16 | 0.17 | 0.17 | 0.16 | 0.16 |
| $MoO_4^{2-}$ | 0.0002 | 0.0002 | 0.0002 | 0.0002 | 0.0002 | 0.0002 |
| $SiO_3^{2-}$ | 0.004 | 0.004 | 0.004 | 0.004 | 0.004 | 0.004 |
| $SO_4^{2-}$ | 0.15 | 0.15 | 0.030 | 0.030 | 0.022 | 0.022 |
| $PO_4^{3-}$ | 0.010 | 0.010 | 0.008 | 0.008 | 0.010 | 0.010 |
| $Cl^-$ | 0.025 | 0.025 | 0.010 | 0.010 | 0.040 | 0.040 |
| $F^-$ | 0.032 | 0.032 | 0.010 | 0.010 | 0.050 | 0.050 |
| $NO_2^-$ | 0.52 | 0.52 | 0.74 | 0.74 | 0.37 | 0.37 |
| $NO_3^-$ | 2.14 | 2.14 | 1.10 | 1.10 | 2.84 | 2.84 |
| $OH^-$ | 1.91 | 1.91 | 3.05 | 3.05 | 1.17 | 1.17 |

*Bounding, or high $K^+$, waste.

equilibration time. This approach yields effective $Cs^+$ isotherms that are needed in a dynamic column model for carousel designs.

Mass-transfer parameters are estimated by analyzing column saturation data from an SRS waste simulant and the waste from the Melton Valley Storage Tank W29 (MVST-W29) at Oak Ridge National Laboratory. All of the MVST-W29 experiments were performed using the same lot of CST pellets and the same feed; only the linear superficial velocity, column diameter, and column length were varied. Numerical simulations based on a pore diffusion model are compared to the experimental data, and the intraparticle diffusivity ($D_p$) (m$^2$/s) is adjusted to obtain effective $D_p$ values for the SRS waste simulant and the MVST-W29 waste. The Stokes-Einstein equation is shown to correlate the values of $D_p$ for the two wastes, according to the viscosities of the wastes. For both wastes, the model yields a close fit to the column data. The MVST-W29 breakthrough curves can be well predicted using the ZAME model with a dilution factor from 0.56 to 0.66. The ZAME model with a dilution factor of 1.0 can explain column data from the SRS.

The equilibrium parameters and mass-transfer parameters determined from preliminary column tests are used in rate-model simulations to obtain carousel designs for treating large-scale SRS waste. The length of the mass-transfer zone determines the required column length of each segment in a three-segment carousel process. The mass-transfer zone is defined as the length of column required to contain the $Cs^+$ concentration wave from 90% of the feed concentration to $1.3\times10^{-6}$ kg/m$^3$ (the required decontamination level). An analysis of the dimensionless groups in the model shows that for a given waste and cesium concentration, the mass-transfer zone length (normalized by the particle radius) depends only on the particle Peclet number. The proportionality constant in this relationship is a function of the $Cs^+$ concentration and the waste composition. Using this linear relationship, one can easily adjust the carousel column size for changes in linear velocity, particle size, and intraparticle diffusivity.

This study establishes a model-based design approach that is efficient and requires few experiments. This approach gives carousel designs with high column utilization both during startup and at cyclic steady state. This method can be applied to the design of carousel ion-exchange processes for other complex wastes.

## Simulation Models, Parameters, and Assumptions

### *Pore diffusion model*

The mathematical model utilized in the simulations is a pore diffusion model that takes into account adsorption, bulk convection, axial dispersion, film mass transfer, and pore diffusion. Competitive adsorption is implicitly taken into account by means of an effective single-component isotherm. The model is useful for validating isotherm and mass-transfer parameters, and for exploring potential designs.

The numerical solutions of the governing equations and boundary conditions are performed by the VERSE simulation package (Whitley, 1990; Berninger et al., 1991). The equations are solved by the method of orthogonal collocation on finite elements in the spatial domain. The DASPK solver is used to integrate in the time domain. This model has been validated in many previous studies (Ma et al., 1996; Ernest et al., 1997; Koh et al., 1998). The model assumes uniform spherical adsorbent particles, plug flow with constant linear velocity, local equilibrium within the adsorbent, and constant diffusivities.

The material balance in the mobile phase is given by

$$\frac{\partial C_b}{\partial t} = E_b \frac{\partial^2 C_b}{\partial z^2} - u_0 \frac{\partial C_b}{\partial z} - \frac{3k_f(1-\epsilon_b)}{R_p \epsilon_b}\left(C_b - C_p|_{r=R_p}\right) \tag{1}$$

$$z = 0, \qquad E_b \frac{\partial C_b}{\partial z} = u_0\left(C_b - C_f(t)\right)$$

$$z = L_c, \qquad \frac{\partial C_b}{\partial z} = 0$$

$$t = 0, \qquad C_b = C_b(z)$$

where $C_b$ is the mobile-phase concentration (kg/m$^3$), $t$ is time (s), $E_b$ is the axial dispersion coefficient (m$^2$/s), $z$ is the axial distance along the column (m), $u_0$ is the mobile-phase interstitial velocity (m/s), $k_f$ is the film mass-transfer coefficient (m/s), $R_p$ is the particle radius (m), and $C_p|_{r=R_p}$ is the pore-phase solute concentration at the surface (kg/m$^3$).

In the pore phase, the material balance equation for a single-solute system is

$$\left(\epsilon_p + (1-\epsilon_p)\frac{\partial Q}{\partial C_p}\right)\frac{\partial C_p}{\partial t} = \epsilon_p \frac{D_p}{r^2}\frac{\partial}{\partial r}\left(r^2 \frac{\partial C_p}{\partial r}\right) \tag{2}$$

$$r = 0, \qquad \frac{\partial C_p}{\partial r} = 0$$

$$r = R_p, \qquad \epsilon_p D_p \frac{\partial C_p}{\partial r} = k_f\left(C_b - C_p\right)$$

$$t = 0, \qquad C_p = C_p(r)$$

**Table 2. Dimensionless Parameters in the Pore Diffusion Model (Eqs. 3 and 4)**

| Parameter | Definition | Description | Value† |
|---|---|---|---|
| $X$ | $zD_p/u_0R_p^2$ | Dimensionless axial distance | 0 to 7.5 |
| $Y$ | $rD_p/u_0R_p^2$ | Dimensionless radial distance | 0 to $4.0\times10^{-4}$ |
| $\tau$ | $tD_p/R_p^2$ | Dimensionless time | $\geq 0$ |
| $\phi_b$ | $(1-\epsilon_b)/\epsilon_b$ | Particle/bulk phase ratio | 1.0 |
| $\phi_p$ | $(1-\epsilon_p)/\epsilon_p$ | Solid/pore phase ratio | 3.2 |
| $L^*$ | $L_c/R_p$ | Dimensionless column length | $1.8\times10^4$ |
| $Pe_a$ | $u_0R_p/E_b$ | Convection/axial dispersion | 0.21 |
| $Pe_p$ | $u_0R_p/D_p$ | Convection/intraparticle diffusion | $2.5\times10^3$ |
| $Sh$ | $k_fR_p/D_p$ | Film mass-transfer/diffusion | 82 |

†ID = 1.22 m; $L_c$ = 3.44 m; $u_0 = 1.6\times10^{-3}$ m/s; $R_p$ = 187.5 $\mu$m; $D_p = 1.2\times10^{-10}$ m$^2$/s.

where $C_p$ is the pore-phase concentration (kg/m$^3$), $Q$ is the solid-phase concentration (kg/m$^3$ S.V.), $r$ is the distance in the radial direction (m), and $D_p$ is the intraparticle diffusivity (m$^2$/s).

For large-particle columns, such as the system under study here, intraparticle diffusion is often the controlling mass-transfer resistance. Therefore, it is useful to normalize the differential mass-balance equations in terms of a characteristic diffusion time ($R_p^2/D_p$) and a characteristic convection length ($u_0R_p^2/D_p$) during the diffusion time. Equations 1 and 2 and their boundary conditions can then be rewritten as follows in terms of the dimensionless quantities listed in Table 2.

*Bulk phase*

$$\frac{\partial C_b}{\partial \tau} = \frac{1}{Pe_a}\frac{1}{Pe_p}\frac{\partial^2 C_b}{\partial X^2} - \frac{\partial C_b}{\partial X} - 3\phi_b Sh\left(C_b - C_p|_{Y=1/Pe_p}\right) \tag{3}$$

$$X = 0, \qquad \frac{\partial C_b}{\partial X} = Pe_a Pe_p\left(C_b - C_f(\tau)\right)$$

$$X = \frac{L^*}{Pe_p}, \qquad \frac{\partial C_b}{\partial X} = 0$$

$$\tau = 0, \qquad C_b = C_b(X)$$

*Pore phase*

$$\left(1 + \phi_p \frac{\partial Q}{\partial C_p}\right)\frac{\partial C_p}{\partial \tau} = \frac{1}{Pe_p^2}\frac{1}{Y^2}\frac{\partial}{\partial Y}\left(Y^2 \frac{\partial C_p}{\partial Y}\right) \tag{4}$$

$$Y = 0, \qquad \frac{\partial C_p}{\partial Y} = 0$$

$$Y = \frac{1}{Pe_p}, \qquad \frac{\partial C_p}{\partial Y} = (1-\phi_p)\, Pe_p Sh\left(C_b - C_p\right)$$

$$\tau = 0, \qquad C_p = C_p(Y)$$

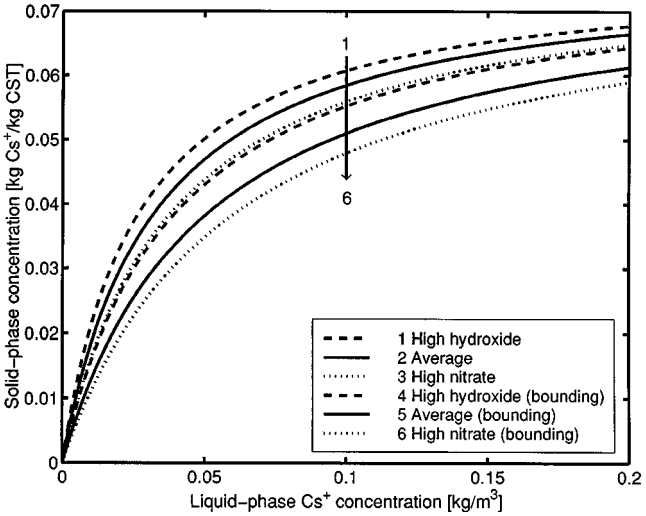


**Figure 2. ZAME model of $Cs^+$ uptake on CST powder for SRS waste simulants.**

*Batch tests for determination of effective $Cs^+$ isotherms in complex wastes*

Figure 2 shows effective $Cs^+$/CST isotherms based on ZAME model predictions for the SRS waste simulants in Table 1. The wastes are complex multicomponent mixtures and the ZAME model is able to predict to within $\pm 10\%$ the effective adsorption capacity of $Cs^+$ at various $Cs^+$ feed concentrations for typical Dept. of Energy waste simulants (Zheng et al., 1997). ZAME model isotherms for different waste compositions are fit to individual Langmuir isotherms of the form $Q = aC/(1 + bC)$, which are implemented in the rate model. The Langmuir isotherm parameters for the SRS waste simulants and for MVST-W29 waste are listed in Table 3. It should be noted that the $a$ values in Table 3 are listed in terms of per solid volume (S.V.) in order to be compatible with the model (Eqs. 3 and 4), whereas the $Q$ values shown in Figures 2 to 4 are in terms of per solid weight. A bed density of 1,000 kg/m$^3$ is used to convert between the two bases.

**Table 3. Langmuir Coefficients for Modeling SRS and MVST-W29 Column Tests**

| Waste | $a$ (m$^3$/m$^3$ S.V.) | $b$ (m$^3$/kg) |
|---|---|---|
| SRS average | 6,310 | 30.9 |
| SRS average, bounding | 4,010 | 19.8 |
| SRS high $OH^-$ | 7,630 | 37.6 |
| SRS high $OH^-$, bounding | 5,150 | 25.3 |
| SRS high $NO_3^-$ | 5,340 | 26.3 |
| SRS high $NO_3^-$, bounding | 3,380 | 16.7 |
| MVST-W29 | 2,230 | 11.9 |

Figure 3a shows the ZAME model predictions for the SRS standard simulant (on CST powder) along with the batch test data for this simulant on CST powder (McCabe, 1995) and CST pellets (McCabe, 1997). The experimental data for the powder are in reasonable agreement with the model predictions. The experimental data for the pellets (IE-910 07398-38B) can be explained by model predictions with a dilution factor between 0.56 and 0.70. This dilution factor is taken into account by multiplying the Langmuir $a$ value in the effective isotherms by the same dilution factor. The maximum capacity (at high concentration) of CST pellets is 56% of that of the powdered form. The apparent dilution factor for the pellet could be due to nonequilibrium data, since the samples in the batch tests in Figure 3a were taken after 48 h. This hypothesis is supported by batch test data obtained on a slightly different waste (SRS "Average" waste simulant) by Hunt et al. (1998), shown in Figure 3b. The batch data collected at 24 and 72 h are not at equilibrium, evident from the time-varying concentration. (There is only a slight increase in $Q$ as $C$ decreases due to the large concentration of $Cs^+$ in the batch experiments.) For these large particles, the equili-

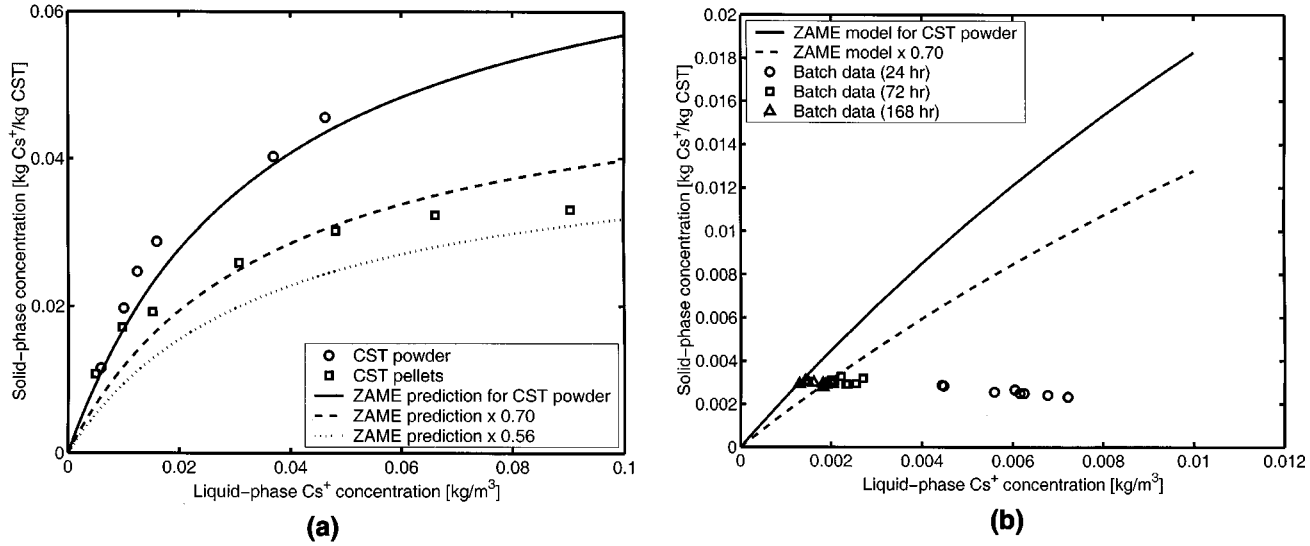


**Figure 3. Experimental $Cs^+$/CST isotherms for SRS waste simulants.**

(a) CST type: IONSIV IE-911 Lot 07398-38B. Feed: SRS high level waste, which is similar to "High $OH^-$" waste but with 2.35 kmol/m$^3$ $NO_3^-$ and 0.00024 kmol/m$^3$ $Cs^+$; (b) $Cs^+$/CST isotherms in SRS "Average" waste. Symbols denote batch samples taken at 24, 72, and 168 h.

bration time should be 168 h or more under the batch test conditions.

### *Column tests for determination of mass-transfer parameters and validation of isotherm parameters*

The isotherm data obtained from batch experiments and the mass-transfer parameters determined from correlations are validated with small- and large-scale column data from Melton Valley Storage Tank W29 (Lee et al., 1997; Walker, Jr. et al., 1998) and small-scale column data from Westinghouse Savannah River Company (Walker et al., 1998).

*Melton Valley Storage Tank W29 Tests.* MVST-W29 waste was used as the feed for several column saturation tests in the Cesium Removal Demonstration (CsRD) runs at Oak Ridge National Laboratory. In Figure 4, the ZAME model for $Cs^+$ uptake on CST powder in the MVST-W29 waste is denoted by a solid line. All of the column data for MVST-W29 waste on CST pellets are well predicted by isotherm parameters represented by the region between the two dotted lines in Figure 4, which correspond to isotherms with maximum capacities that are 56% and 66%, respectively, of that of the CST powder. Since MVST-W29 waste is not a simulant, this dilution factor could be due to the presence of competing ions in the real waste (such as Zn, Pb, and Ba) that are not considered in the ZAME model and other factors discussed later.

When the equilibrium parameters are validated, the only unknown in the analysis of the column tests is the mass-transfer resistance. The Brownian diffusivity for MVST-W29 waste is taken from the work of Ernest et al. (1997). The film mass-transfer coefficient $k_f$ (m/s) is calculated from the correlation by Wilson and Geankoplis (1966), and the axial dispersion coefficient $E_b$ is calculated from the correlation by Chung and Wen (1968). The intraparticle diffusivity $D_p$ is then fit to the small-scale column saturation data. Figures 5a to 5c show the comparison of experimental data to simulation results for small-scale CsRD support runs by D. Lee. One could use the 50% breakthrough point to determine effective isotherm parameters, but this reference point is not representative of the equilibrium retention time if the breakthrough curve is asymmetric. The entire breakthrough curve is well predicted using these isotherm and mass-transfer parameters, indicating that both sets of parameters are valid.

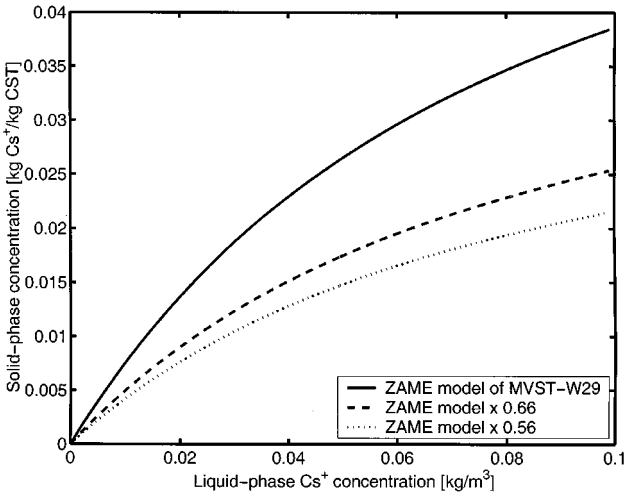


**Figure 4. $Cs^+$/CST isotherm for MVST-W29 waste.**

Solid line denotes the ZAME model of $Cs^+$ uptake on CST powder. Dashed lines represent the upper and lower bounds of isotherms that predict column data on pelletized CST in MVST-W29 waste.

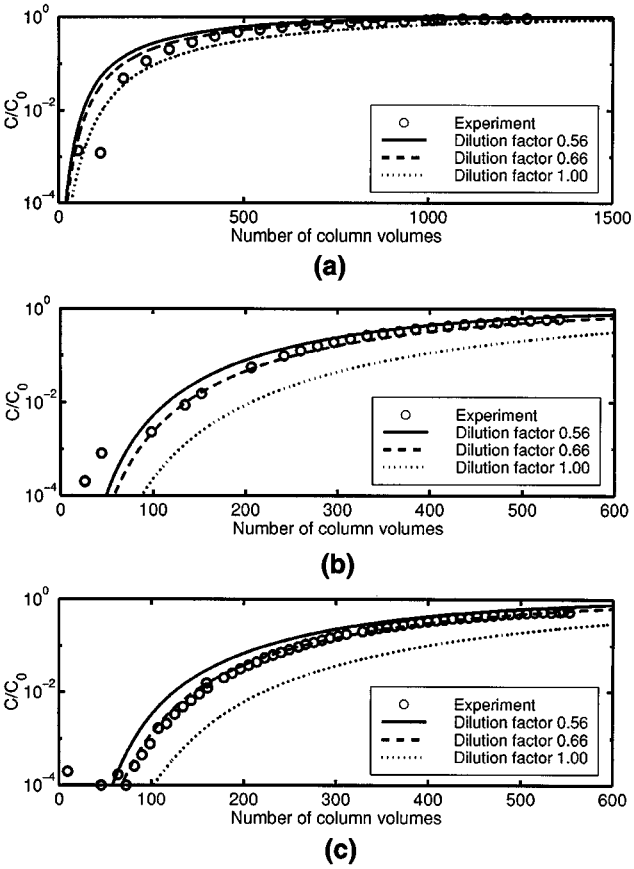


**Figure 5. MVST-W29 small-scale column experiments compared to simulation.**

$D_p = 1.7\times10^{-10}$ m$^2$/s. ID = 0.0145 m. (a) $L_c = 0.0610$ m. $u_s = 1.0\times10^{-4}$ m/s; (b) $L_c = 0.0759$ m. $u_s = 6.3\times10^{-5}$ m/s; (c) length: 0.140 m total for two columns. $u_s = 2.3\times10^{-4}$ m/s.

These parameters determined from the analysis of small-scale experiments are then used to predict the large-scale frontal data, and it is found that the large-scale breakthrough curves are slightly more spread than predicted by the model. Figures 6 and 7 show a comparison of experiment to simulation for large-scale MVST-W29 column experiments. There is some gap between the experimental data and the model predictions using parameters from the small-scale experiments. The column in Figure 6 was initially backwashed with MVST-W29 supernate. $Cs^+$ adsorbed on the binder or the surface of the CST may have leached off the bottom of the column. This may have resulted in high values of the $Cs^+$ concentration in the first few samples. There can also be more dispersion in large columns than in small columns, perhaps as a result of different packing procedures. As shown in Figure 6, an axial dispersion coefficient that is 100 times that predicted by the Chung and Wen correlation can give closer

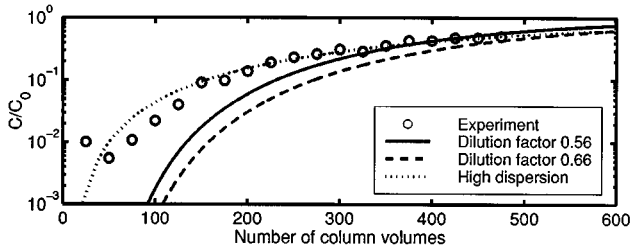


**Figure 6. MVST-W29 large-scale column experiment compared to simulation.**

$D_p = 1.7\times10^{-10}$ m$^2$/s. $L_c = 0.538$ m. ID = 0.30 m. $u_s = 4.5\times10^{-4}$ m$^3$/s. The cases denoted by dilution factor 0.56 and 0.66 have $E_b$ predicted by the Chung and Wen correlation. The high dispersion case has a dilution factor of 0.66 and $E_b = 100$ times the prediction by the Chung and Wen correlation.

agreement with the breakthrough data, especially at early times. Another possibility is slow equilibration, which has a significant effect at high linear velocity (in Figure 6, $u_s = 9.0\times10^{-4}$ m/s). Simulations based on a smaller $D_p$ ($1.0\times10^{-10}$ m$^2$/s) are almost identical as the large $E_b$ results (not shown). At small contact times, the solute can have a smaller effective capacity for the exchanger, which can lead to a low apparent diffusion coefficient (Whitley et al., 1993). However, more data at higher linear velocities are needed to confirm this hypothesis.

*Westinghouse Savannah River Company Tests.* Since MVST-W29 waste has a viscosity of 1.6 cp and SRS waste has a viscosity of 2.2 cp, the value of $D_p$ determined from the MVST-W29 column tests is not valid for designing columns to handle SRS waste. According to the Stokes-Einstein equation, the diffusivity is inversely related to the solution viscosity as follows:

$$D = \frac{k_B T}{6\pi\mu R_0} \tag{5}$$

where $D$ is the diffusivity (m$^2$/s), $k_B$ is Boltzmann's constant, $T$ is absolute temperature (K), $\mu$ is the viscosity (kg/m·s), and $R_0$ is the solute radius (m). According to Eq. 5, the intraparticle diffusivity for SRS wastes is estimated to be $1.7\times10^{-10}\times(1.6/2.2) = 1.2\times10^{-10}$ m$^2$/s. The Brownian diffusivity is reduced by the same factor. The mass-transfer zone length, as will be shown later, is inversely proportional to the intraparticle diffusivity. Therefore, the mass-transfer zone length is linearly proportional to viscosity. In Figure 8, one can see that the intraparticle diffusivity corrected by the Stokes-Einstein correlation (solid line) predicts the column data better than the uncorrected diffusivity (dashed line).

Preliminary column data have been obtained for SRS "Average" waste simulant on CST pellets (Walker et al., 1998b). The column experiments can be well predicted assuming a dilution factor of 1.0 and a $D_p$ value of $1.2\times10^{-10}$ m$^2$/s. Figure 8 shows column effluent histories for three

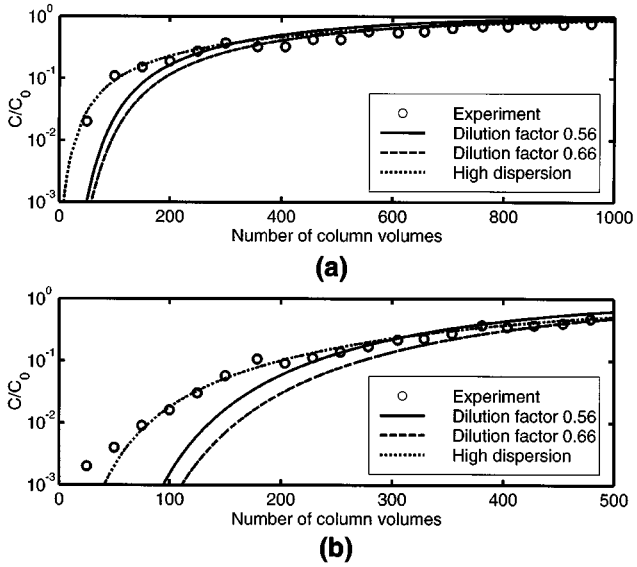


**Figure 7. MVST-W29 large-scale two-column experiment compared to simulation.**

$D_p = 1.7\times10^{-10}$ m$^2$/s. Length: 1.08 m total for two columns. ID = 0.30 m. $u_s = 9.0\times10^{-4}$ m/s. See Figure 6 for an explanation of the high dispersion case. (a) Lead column effluent history; (b) second column effluent history.

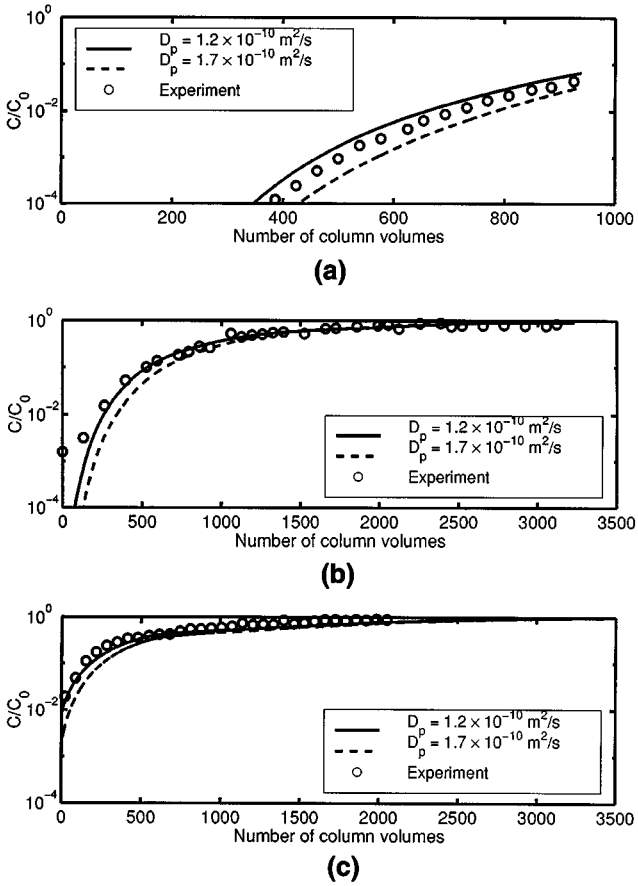


**Figure 8. SRS column experiments compared to simulation.**

Feed: SRS "Average" simulant (Table 1). Dilution factor: 1.0. (a) $L_c = 0.10$ m. ID = 0.015 m. $u_s = 4.5\times10^{-5}$ m/s; (b) $L_c = 0.10$ m. ID = 0.015 m. $u_s = 1.6\times10^{-4}$ m/s; (c) $L_c = 0.11$ m. ID = 0.014 m. $u_s = 6.8\times10^{-4}$ m/s.

runs in laboratory-scale columns ( ~ 0.015 m in diameter and ~ 0.10 m in length) at three different linear superficial velocities ($u_s = 4.5\times10^{-5}$, $1.63\times10^{-4}$, and $6.8\times10^{-4}$ m/s). There is some gap between model and experiment in Figure 8a at early times, but this is because the $Cs^+$ concentrations at these times is below the detection limit of the analytical method. Because the ion exchanger cannot be regenerated by practical means, the packing in each of these three column tests may be slightly different. This can help explain why the model predicts a slightly earlier breakthrough than the data in Figure 8a and lags slightly behind the data in Figure 8c. The isotherm parameters, mass-transfer model, and the correlation of $D_p$ using the Stokes-Einstein equation appear to be valid over the linear velocity range from $u_s = 4.5\times10^{-5}$ to $6.8\times10^{-4}$ m/s.

### *Column parameters*

The particle size, interparticle void fraction ($\epsilon_b = 0.50$), and intraparticle void fraction ($\epsilon_p = 0.24$) are based on the known densities of the CST particles (Huckman et al., 1999). In the mathematical model, it is assumed that all of the particles are spherical and are of uniform size (375 $\mu$m in diameter). These system parameters and the mass-transfer parameters above are used in the design of large-scale carousel processes for treating SRS wastes.

## Design Approach

### *Determination of the constant-pattern mass-transfer zone length*

The first step in the design is to determine the constant-pattern mass-transfer zone length, which is a function of the isotherm parameters, $Cs^+$ feed concentrations, mass-transfer parameters, and linear velocity. The isotherm and mass-transfer parameters used in this design are the same as those used in the analysis of the SRS column data (Figure 8). A dilution factor of 1.0 is assumed. The mass-transfer zone length is examined at two different flow rates—$9.5\times10^{-4}$ and $1.6\times10^{-3}$ $m^3$/s, which correspond to two different superficial velocities ($8.2\times10^{-4}$ and $1.4\times10^{-3}$ m/s, respectively).

In determining the mass-transfer zone, which spans four orders of magnitude of concentration, it is important to verify the convergence of the numerical solution. For the column profiles in this study, the column length (20 m) is divided into 600 axial elements with four collocation points per element, and the particle phase associated with each axial element is represented by one element with four collocation points. For time integration, which is performed by the DASPK package, the absolute tolerance on local solutions is $10^{-7}$ kg/$m^3$ and the relative tolerance is $10^{-4}$. The step-size for time integration is determined by DASPK automatically. The user-defined maximum step-size is set to 10 bed volumes. These numerical parameters yield robust solutions. Simulations with tighter numerical parameters—1,000 axial elements, six collocation points per axial element, five collocation points per particle element, an absolute tolerance of $5\times10^{-8}$ kg/$m^3$, and a relative tolerance of $10^{-5}$—when changed individually, change the mass-transfer zone length by 1% or less.

Since the isotherm is nonlinear at the concentration level in the SRS waste (Figure 2), each concentration wave eventually develops into a constant pattern. Numerical simulations based on the validated rate model described in Eqs. 3 and 4 are employed to determine the design. A sufficiently long column (20 m) is chosen in these simulations so that the waves can reach a constant pattern. Figure 9 demonstrates the mass-transfer zone length determination. The length of the mass-transfer zone is determined from the concentration profile where the local concentration decreases from 90% of the feed concentration to $1.3\times10^{-6}$ kg/$m^3$. It is assumed that a constant pattern has been achieved when $L_{MTZ}$ changes by less than 1% over 180 bed volumes. The feed compositions are listed in Table 1. Note that the concentration of $Cs^+$ and the effective isotherm vary from waste to waste. For this specification, the percent saturation in the lead column is

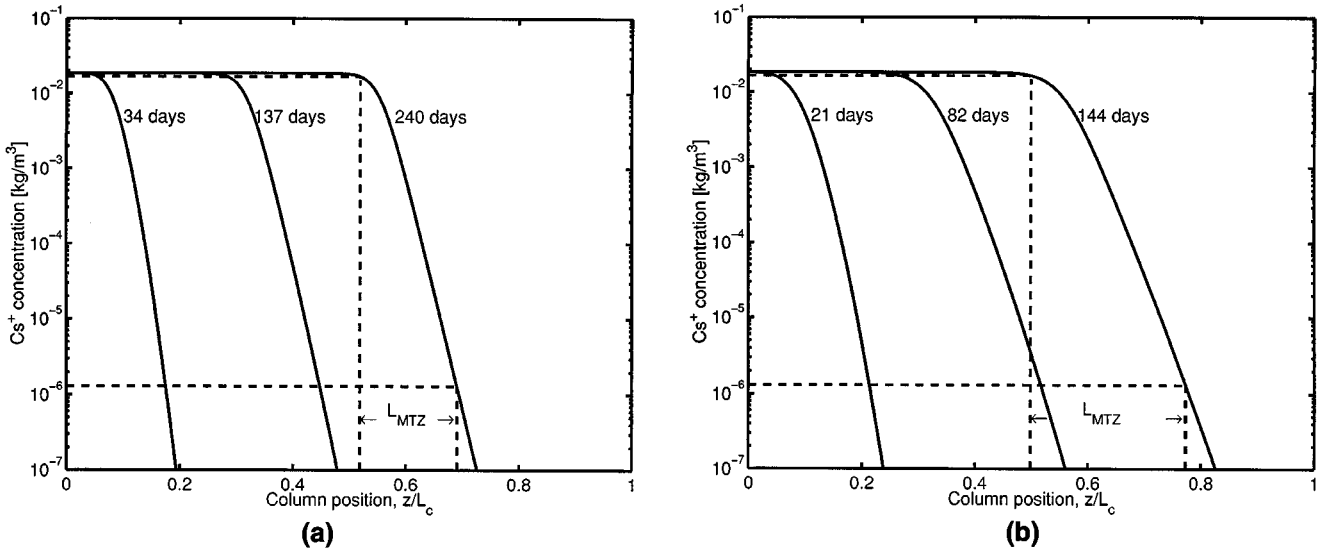


**Figure 9. Mass-transfer zone length determination.**

Feed: SRS "Average" simulant. $D_p = 1.2\times10^{-10}$ $m^2$/s. $L_c = 20$ m. ID = 1.22 m. (a) $u_s = 8.2\times10^{-4}$ m/s; (b) $u_s = 1.4\times10^{-3}$ m/s.

**Table 4. Column Length Requirement for a Fixed Column Diameter of 1.22 m**

| SRS Waste Simulant | Flow Rate ($m^3/s$)$\times 10^4$ | $u_s$ (m/s)$\times 10^3$ | $u_0$ (m/s)$\times 10^3$ | $Pe_p$ | $L_{MTZ}$ (m) |
|---|---|---|---|---|---|
| Average | 9.5 | 0.82 | 1.6 | $2.50\times 10^3$ | 3.4 |
| | 16 | 1.4 | 2.7 | $4.16\times 10^3$ | 5.7 |
| Average* | 9.5 | 0.82 | 1.6 | $2.50\times 10^3$ | 1.6 |
| | 16 | 1.4 | 2.7 | $4.16\times 10^3$ | 2.7 |
| High $OH^-$ | 9.5 | 0.82 | 1.6 | $2.50\times 10^3$ | 1.6 |
| | 16 | 1.4 | 2.7 | $4.16\times 10^3$ | 2.6 |
| High $OH^-$* | 9.5 | 0.82 | 1.6 | $2.50\times 10^3$ | 1.4 |
| | 16 | 1.4 | 2.7 | $4.16\times 10^3$ | 2.3 |
| High $NO_3^-$ | 9.5 | 0.82 | 1.6 | $2.50\times 10^3$ | 3.9 |
| | 16 | 1.4 | 2.7 | $4.16\times 10^3$ | 6.4 |
| High $NO_3^-$* | 9.5 | 0.82 | 1.6 | $2.50\times 10^3$ | 1.8 |
| | 16 | 1.4 | 2.7 | $4.16\times 10^3$ | 3.0 |

SRS wastes are defined in Table 1.
*Bounding, or high $K^+$, case.
$R_p = 187.5\ \mu$m; $D_p = 1.2\times 10^{-10}$ $m^2/s$; dilution factor: 1.0.

much higher than 90% (the target for large-scale applications). Clearly, the mass-transfer zone length $L_{MTZ}$ increases with increasing column length and reaches a maximum value when a constant pattern develops.

If one chooses the constant-pattern $L_{MTZ}$ to be the segment length in a carousel, the design is straightforward. A three-segment carousel has a total length of $3L_{MTZ}$. The choice of constant-pattern $L_{MTZ}$ to be the segment length will ensure high column utilization, during the startup period and at cyclic steady state. The percent sorbent utilization in the lead column (saturation zone) will satisfy the specification of a 90% or higher utilization. VERSE simulations, in which discontinuities due to port switching can be taken into account, are employed to confirm the validity of this approach as discussed below.

### *Carousel designs for a fixed column diameter*

For practical applications, a column diameter of about 1.22 m (4 ft) and a segment length of 4.88 m (16 ft) or smaller are desired. Table 4 lists the column length requirements for the six SRS waste simulants when the column diameter is fixed at 1.22 m. For each isotherm, we have determined the mass-transfer zone lengths for two flow rates, $9.5\times 10^{-4}$ $m^3/s$ (15 gal/min) and $1.6\times 10^{-3}$ $m^3/s$ (25 gal/min), by the procedure outlined above.

In determining the length of an individual segment of a carousel bed, simulations of a single column are used. As a check on the design approach, carousel simulations that take into account concentration discontinuities between columns are carried out. The simulations take into account discontinuities in concentration that occur between columns at the time of port switching, whereas in the design step these discontinuities are neglected. In the carousel process simulations, the port switching occurs when the outlet concentration of the second column reaches $1.3\times 10^{-6}$ $kg/m^3$. At this time, the first column is taken off-line, the feed is introduced into the second column, and a fresh column is introduced at the end of the train (as a guard column).

**Table 5. System and Mass-Transfer Parameters Used in Carousel Simulations**

| Parameter | Value at $9.5\times 10^{-4}$ $m^3/s$ | Value at $1.6\times 10^{-3}$ $m^3/s$ | Source |
|---|---|---|---|
| ID (m) | 1.2 | 1.3 | |
| $L_c$ (m) | 3.44 | 4.88 | |
| Switching time (d) | 74 | 73 | |
| $R_p$ ($\mu$m) | 187.5 | 187.5 | McCabe (1995) |
| $\epsilon_b$ | 0.50 | 0.50 | Huckman et al. (1999) |
| $\epsilon_p$ | 0.24 | 0.24 | Huckman et al. (1999) |
| $D^\infty$ ($m^2/s$) | $1.6\times 10^{-9}$ | $1.6\times 10^{-9}$ | Ernest et al. (1997) |
| $D_p$ ($m^2/s$) | $1.2\times 10^{-10}$ | $1.2\times 10^{-10}$ | |
| $k_f$ (m/s) | $5.27\times 10^{-5}$ | $5.95\times 10^{-5}$ | Wilson-Geankoplis (1966) |
| $E_b$ ($m^2/s$) | $1.47\times 10^{-6}$ | $2.12\times 10^{-6}$ | Chung and Wen (1968) |
| % Utilization | 99 | 99 | |

For the "Average" waste, a throughput of $9.5\times 10^{-4}$ $m^3/s$ requires a three-column carousel that is 1.22 m in diameter and 3.44 m in segment length, while a throughput of $1.6\times 10^{-3}$ $m^3/s$ requires a carousel that is 1.3 m in diameter and 4.9 m in segment length. The operating parameters for such processes are listed in Table 5. Figure 10 shows the simulated concentration histories at the outlet of each column in a typical carousel process operated at $9.5\times 10^{-4}$ $m^3/s$. Note that the outlet concentration of column 2 reaches the specified value of $1.3\times 10^{-6}$ $kg/m^3$ at the port switching time. The outlet concentration of column 3 (the guard column) is too low to be seen in this figure. Figure 10 also shows that cyclic steady state is established after about three switching periods. The column utilization is calculated as

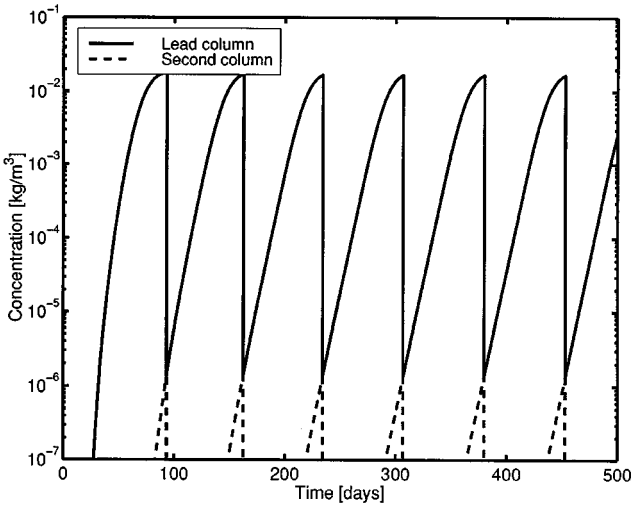


**Figure 10. Simulated $Cs^+$ concentration histories at each outlet port in a three-column carousel process.**

The outlet concentration of the third column is below $10^{-7}$ $kg/m^3$. Feed: SRS "Average" simulant. $D_p = 1.2\times 10^{-10}$ $m^2/s$. Length: 10.3 m total for three columns. ID = 1.22 m. $u_s = 8.1\times 10^{-4}$ m/s.

$$\text{utilization} = \frac{\int_0^{L_c} C_b(z)\,dz}{L_c C_f} \times 100\% \qquad (6)$$

The utilization of the lead column is about 99.8% before cyclic steady state is established and 99.2% at cyclic steady state. This result indicates that by choosing the constant-pattern $L_{MTZ}$, one can ensure high utilization during startup and after cyclic steady state is established. It is apparent from Figure 10 that the constant-pattern mass-transfer zone length determined from the single long column can be used as the single-segment length in a three-segment, discontinuous carousel process.

### *Analysis of mass-transfer zone length and its relation to particle Peclet number and isotherm nonlinearity*

By examining the differential mass balance equations and boundary conditions (Eqs. 3 and 4), one expects that the concentration profile or dimensionless mass-transfer zone length $L_{MTZ}/R_p$ at constant pattern is a function of the dimensionless groups of the equations ($L^*$, $\phi_b$, $\phi_p$, $Sh$, $Pe_a$, and $Pe_p$), the isotherm parameters, and the feed concentration of $Cs^+$. For a sufficiently long column ($L_c/R_p > 1{,}000$) at a relatively high linear velocity ($u_0 > 5\times10^{-4}$ m/s), wave spreading is controlled by intraparticle diffusion. Therefore, $L_{MTZ}/R_p$ is expected to be only a function of $Pe_p$ for a given waste. This relationship can be summarized as

$$\frac{L_{MTZ}}{R_p} \propto Pe_p \quad \text{or} \quad L_{MTZ} \propto R_p Pe_p \qquad (7)$$

Equation 7 states that the length of the mass-transfer zone is directly proportional to the linear velocity and the square of the particle radius, and that it is inversely proportional to the intraparticle diffusivity. This relationship can be explained as follows. If intraparticle diffusion is the rate-controlling step, a characteristic diffusion time is $R_p^2/D_p$. During the diffusion time, convection can spread a concentration wave over a distance of $u_0 R_p^2/D_p$. Therefore, $L_{MTZ}$ is proportional to $R_p Pe_p$.

Figure 11a shows the relationship between the dimensionless mass-transfer zone and the Peclet number. The slope of the line in each case depends on both the waste type and the cesium concentration. By changing the composition of the non-$Cs^+$ components, one can change the viscosity and the intraparticle diffusivity. Figure 11a provides a convenient estimate of $L_{MTZ}$ (or carousel size) when $R_p$, $D_p$, or $u_0$ is varied.

The slopes of straight lines in Figure 11a are different for the different wastes because of different degrees of isotherm nonlinearity. To show the effects of isotherm nonlinearity ($bC_f$) on $L_{MTZ}$, the results in Figure 11a are compared with the predictions from an analytical solution for constant pattern waves obtained from a linear driving force model (Michaels, 1952; Hall et al., 1966; Garg and Ruthven, 1973; Ruthven, 1984; Wankat, 1994). In this model, all resistances are lumped into an overall mass-transfer coefficient $K_f$, which is assumed to be a constant. The differential mass balance for the particle phase in the linear driving-force model can

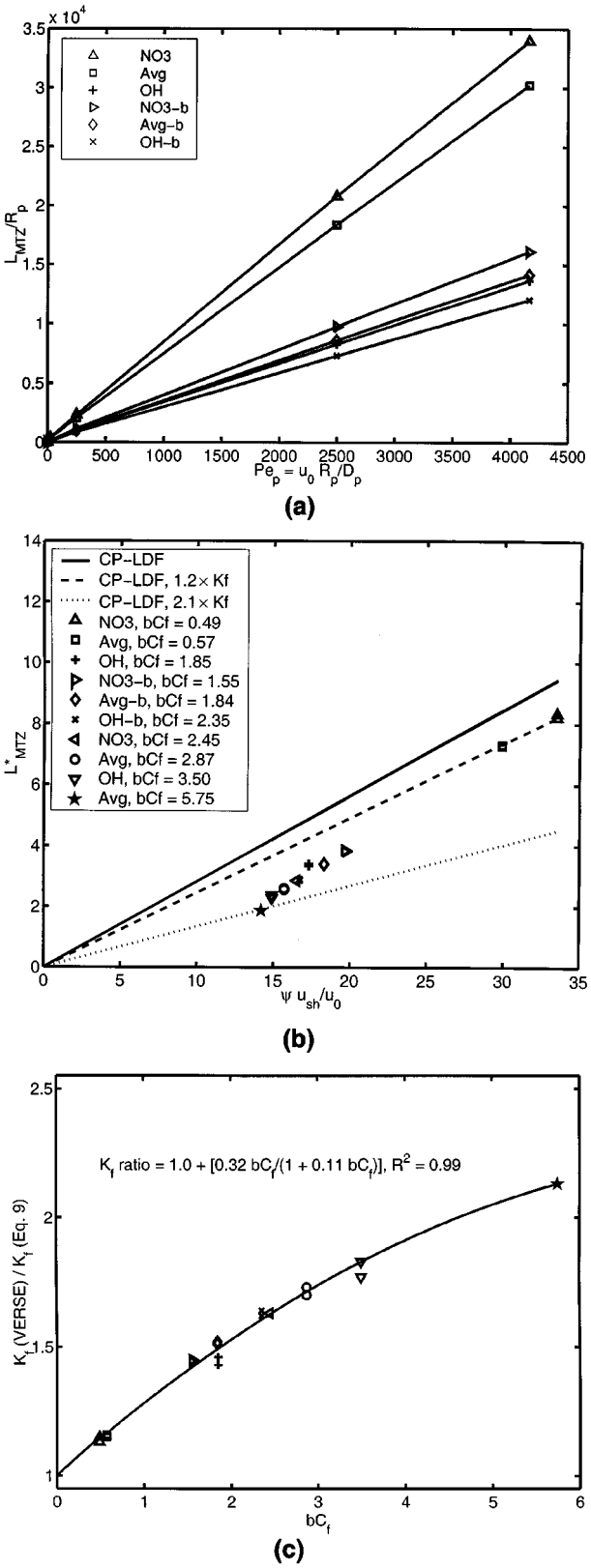


**Figure 11. Analysis of dimensionless groups.**

(a) Dimensionless mass-transfer zone length (calculated by the pore diffusion model) as a function of the Peclet number; (b) comparison of scaled mass-transfer zone length as calculated by the pore diffusion model and the constant-pattern linear driving force (CP-LDF) solution; (c) effective $K_f$ ratio as a function of isotherm nonlinearity ($bC_f$).

be written as follows

$$\frac{\partial Q_p}{\partial t} = K_f(C_b - C_b^*) \tag{8}$$

The term $C_b^*$ represents the bulk-phase solute concentration in equilibrium with the particle-phase concentration, and $K_f$ represents the lumped mass-transfer coefficient. For linear isotherm systems, this can be expressed as (Ruthven, 1984)

$$\frac{1}{K_f} = \frac{E_b}{u_0^2}\left(\frac{1-\epsilon_b}{\epsilon_b}\right) + \frac{R_p}{3k_f} + \frac{R_p^2}{15\epsilon_p D_p} \tag{9}$$

If intraparticle diffusion is controlling, only the last term in Eq. 9 is important. Integrating Eq. 8 between the low-concentration end of the constant-pattern wave $C_1 = \phi_1 C_f$, and the high-concentration end $C_2 = \phi_2 C_f$, and multiplying by the shockwave velocity, yields the $L_{\mathrm{MTZ}}$ for a constant-pattern wave in a column that is initially clean (that is, $C_b(0, z) = 0$)

$$L_{\mathrm{MTZ}} = \frac{u_0}{1 + \dfrac{1-\epsilon_b}{\epsilon_b}\dfrac{a_p}{1+bC_f}}\left(\frac{a_p}{1+bC_f}\right)\left(\frac{1}{K_f}\right) \times \left[\frac{1}{bC_f}\ln\left(\frac{\phi_2(1-\phi_1)}{\phi_1(1-\phi_2)}\right) + \ln\left(\frac{\phi_2}{\phi_1}\right)\right] \tag{10}$$

The Appendix provides the details of this derivation. In the present system $\phi_2 = 0.90$ and $\phi_1$ can take on values from $1.4\times10^{-5}$ to $7.0\times10^{-5}$ depending on the feed concentration.

If one defines the distribution coefficient at the feed concentration as $K_d^f = a_p/(1+bC_f)$, then Eq. 10 can be rewritten as

$$L_{\mathrm{MTZ}} = \frac{u_0 K_d^f}{1 + \dfrac{1-\epsilon_b}{\epsilon_b}K_d^f}\left(\frac{1}{K_f}\right) \times \left[\frac{1}{bC_f}\ln\left(\frac{\phi_2(1-\phi_1)}{\phi_1(1-\phi_2)}\right) + \ln\left(\frac{\phi_2}{\phi_1}\right)\right] \tag{11}$$

In general, Eq. 11 states that $L_{\mathrm{MTZ}}$ is a complex function of $K_d^f$, the zone definition ($\phi_1$, $\phi_2$), and the isotherm nonlinearity ($bC_f$). One can see from Eq. 11 that when $K_d^f \ll 1$, $L_{\mathrm{MTZ}}$ is directly proportional to $K_d^f$. When $K_d^f \gg 1$, the influence of $K_d^f$ is less significant because $K_d^f$ in the numerator of Eq. 11 cancels with $K_d^f$ in the denominator. Because the present system has $K_d^f \sim 1{,}000$ it is expected that $K_d^f$ is relatively unimportant in the determination of $L_{\mathrm{MTZ}}$. The influence of $\phi_1$ and $\phi_2$ is straightforward: a higher value of $\phi_2$ or a lower value of $\phi_1$ results in a larger $L_{\mathrm{MTZ}}$. As isotherm nonlinearity ($bC_f$) increases, the term $1/bC_f$ in Eq. 11 decreases, resulting in a corresponding decrease in $L_{\mathrm{MTZ}}$.

If one defines the following dimensionless variables

$$\frac{u_{sh}}{u_0} = \frac{1}{1 + \dfrac{1-\epsilon_b}{\epsilon_b}\dfrac{a_p}{1+bC_f}} \tag{12}$$

$$\psi = \left(\frac{a_p}{1+bC_f}\right)\left[\frac{1}{bC_f}\ln\left(\frac{\phi_2(1-\phi_1)}{\phi_1(1-\phi_2)}\right) + \ln\left(\frac{\phi_2}{\phi_1}\right)\right] \tag{13}$$

$$L_{\mathrm{MTZ}}^* = \frac{L_{\mathrm{MTZ}}}{R_p Pe_p} \tag{14}$$

then Eq. 11 becomes

$$L_{\mathrm{MTZ}}^* = \left(\frac{D_p}{R_p^2 K_f}\right)\frac{\psi u_{sh}}{u_0} \tag{15}$$

A plot of $L_{\mathrm{MTZ}}^*$ vs. $\psi u_{sh}/u_0$ should yield a straight line with a slope of $D_p/R_p^2 K_f$ if $K_f$ is a constant. The solutions based on Eqs. 9 and 15 can be compared to the numerical solutions obtained from the more detailed pore diffusion model (Figure 11b). Both models yield similar trends (as isotherm nonlinearity increases, $L_{\mathrm{MTZ}}$ decreases). Note that the data shown in Figure 11b are pore diffusion model results calculated from different wastes, which have different $a$, $b$, $C_f$, $\phi_1$, and $\phi_2$ values. If the equivalent $K_f$ is constant, all of the points in Figure 11b should fall on a single straight line. However, the results in Figure 11b indicate that the pore diffusion model gives a smaller $L_{\mathrm{MTZ}}^*$ than predicted from Eqs. 9 and 15. Moreover, as the isotherm nonlinearity ($bC_f$) increases, the equivalent $K_f$ from the pore diffusion model increases from 15 to 120% of the $K_f$ values from Eq. 9. In Figure 11c, the ratio of the effective $K_f$ calculated from VERSE simulations to the $K_f$ calculated from Eqs. 9 and 15 is shown to be a function of $bC_f$. The $y$-intercept based on a least-squares fit to this correlation is 1.0, which indicates that the two models give the same solution in the linear limit ($bC_f \rightarrow 0$).

The differences between the two models for nonlinear systems can be explained by the different assumptions for the two models. The constant pattern solution of the linear driving force model is based on the assumptions that: (1) there is no concentration gradient within particles; (2) the distribution coefficient between the bulk and the particle phase is fixed at the $K_d$ value at the feed concentration $K_d^f$; and (3) $K_f$ is a constant and can be estimated from the equation for linear isotherm systems (Eq. 9). In contrast, the pore diffusion model takes into account the concentration gradients within particles. Since the distribution coefficient increases as the concentration decreases within the particles, the average $K_d$ within the mass-transfer zone is greater than $K_d^f$ and a higher driving force can exist between the bulk and the particle phases than the linear driving force model predicts. As a result, the breakthrough curves are sharper and a higher equivalent $K_f$ is obtained from the porous model.

Figures 11b and 11c provide an estimate of $L_{\mathrm{MTZ}}^*$ when isotherm ($a, b$), feed concentration ($C_f$), particle size, flow rate, and zone definition ($\phi_1$, $\phi_2$) are varied. For a given feed concentration, Figure 11c can be used to determine the equivalent $K_f$ value to be used in the constant pattern solu-

tion. Then, for specified isotherm parameters, mass-transfer zone definition, particle size, intraparticle diffusivity, and flow rate, Figure 11b can be used to determine $L_{MTZ}$.

### *Carousel designs for a fixed column length*

For the six different SRS waste simulants, if the column diameter is fixed at 1.22 m, the segment lengths (or $L_{MTZ}$) are less than 4.88 m with two exceptions: the cases with $1.6\times 10^{-3}$ $m^3/s$ for the "Average" waste and the "High $NO_3^-$" waste (Table 5). For these two wastes and others, we investigate the designs with a fixed segment length of 4.88 m (and a diameter that is large enough to handle the two desired feed flow rates). The results are reported in Table 6. When the segment length is fixed at 4.88 m, this implies that $L_{MTZ}$ is fixed at 4.88 m for all the different feeds; the linear velocity $u_0$ is varied to achieve this goal. The $u_0$ values are determined by finding the Peclet number in Figure 11a that gives $L_{MTZ} = 4.88$ m for a given SRS waste composition. Column diameters that can handle $9.5\times 10^{-4}$ and $1.6\times 10^{-3}$ $m^3/s$ are calculated according to a given $u_0$ (Table 6). Notice that for a given feed, the linear velocity is kept the same for the two volumetric flow rates. A change in the column diameter allows for a change in the volumetric flow rate. Since $L_{MTZ}$ is proportional to $u_0 R_p^2/D_p$, the throughput per bed volume ($u_0/L_{MTZ}$) is proportional to $D_p/R_p^2$ and independent of $u_0$. For this reason, for a given waste composition, designs for a fixed column diameter (Table 4) or a fixed column length (Table 6) have the same throughput per bed volume.

### *Design alternatives*

There are many alternative carousel designs that can meet SRS waste treatment requirements. The sizes of the carousel columns in Tables 4 and 6 are estimated based on a fixed diameter for Case 1, a fixed segment length for Case 2, and the following assumptions: (1) The effective $Cs^+$ isotherms of the wastes can be predicted by using the ZAME model with a dilution factor of 1.0; (2) the $D_p$ value is $1.2\times 10^{-10}$ $m^2/s$ for all wastes; (3) the $L_{MTZ}$ is defined as the length in which $C_b$ decreases from $0.9C_f$ to $1.3\times 10^{-6}$ $kg/m^3$. This definition results in 99.8% utilization during startup and 99.2% at cyclic steady state. One can choose a shorter $L_{MTZ}$ if a lower percent utilization of the lead column is desired or the level of $Cs^+$ in the effluent of column 2 can be higher than $1.3\times 10^{-6}$ $kg/m^3$; (4) three columns are used for purification: the lead column is for saturation, the second column is to contain the mass-transfer zone, and the third column is a guard column. Each column length is the same as the mass-transfer zone length.

Alternatively, the mass-transfer zone can be spread among two columns, thus halving the size of each column in the process. The saturation zone and the guard zone decrease in length (by half), while the mass-transfer zone length remains fixed, leading to a shorter overall bed length. Table 7 compares the performances of carousel processes with three, four, five, and six column segments. One can see that on increasing the number of segments from three to four there is a 50% gain in the throughput per bed volume and a 33% decrease in the bed length. However, there is also a 50% smaller guard column and one more valve. These factors need to be taken into account in future cost analyses and process optimization studies.

**Table 6. Column Diameter Requirement for a Fixed Column-Segment Length of 4.88 m**

| SRS Waste Simulant | Flow Rate $(m^3/s)\times 10^4$ | $u_s$ $(m/s)\times 10^3$ | $u_0$ $(m/s)\times 10^3$ | ID (m) |
|---|---|---|---|---|
| Average | 9.5 | 1.2 | 2.4 | 1.0 |
| | 16 | 1.2 | 2.4 | 1.3 |
| Average* | 9.5 | 2.5 | 5.0 | 0.70 |
| | 16 | 2.5 | 5.0 | 0.91 |
| High $OH^-$ | 9.5 | 2.6 | 5.1 | 0.67 |
| | 16 | 2.6 | 5.1 | 0.88 |
| High $OH^{-}$* | 9.5 | 2.9 | 5.8 | 0.64 |
| | 16 | 2.9 | 5.8 | 0.82 |
| High $NO_3^-$ | 9.5 | 1.0 | 2.1 | 1.0 |
| | 16 | 1.0 | 2.1 | 1.4 |
| High $NO_3^{-}$* | 9.5 | 2.2 | 4.4 | 0.73 |
| | 16 | 2.2 | 4.4 | 0.94 |

*Bounding, or high $K^+$, case.
$R_p = 187.5$ $\mu$m. $D_p = 1.2\times 10^{-10}$ $m^2/s$.

**Table 7. Comparison of Carousel Configurations with Varying Numbers of Segments**

| No. of Segments | Total Bed Length | Relative Throughput | Guard Column Length | No. of Valves |
|---|---|---|---|---|
| 3 | 3 $L_{MTZ}$ | 1 | $L_{MTZ}$ | 3 |
| 4 | 2 $L_{MTZ}$ | 1.5 | 0.50 $L_{MTZ}$ | 4 |
| 5 | 1.67 $L_{MTZ}$ | 1.8 | 0.33 $L_{MTZ}$ | 5 |
| 6 | 1.5 $L_{MTZ}$ | 2.0 | 0.25 $L_{MTZ}$ | 6 |

Column cross-sectional and flow rate are fixed.

## Conclusions

A model-based approach has been developed to design a CST carousel ion-exchange process for removing cesium from Savannah River Site wastes. Batch equilibrium data have been correlated using a detailed ion-exchange model for CST powder (ZAME model). The ZAME model predictions have been fit to the Langmuir equation to obtain effective cesium isotherms for six representative SRS waste compositions. For CST pellets in simulated SRS wastes, a dilution factor of 1.0 can fit the batch test data obtained at 168 h and column data at these different velocities. For MVST-W29 waste, which contains many contaminants that are not present in waste simulants, a dilution factor of 0.56 to 0.66 is needed in order to fit the column data. Axial dispersion and film mass-transfer coefficients are calculated from well-known correlations, and the intraparticle diffusivity is determined by fitting rate model predictions to MVST-W29 and SRS column data. The intraparticle diffusivities for the two wastes can be well correlated by the Stokes-Einstein equation. The effective isotherm approach and the isotherm and mass-transfer parameters have been validated with column data from MVST-W29 waste and SRS waste over a range of linear velocities from $4.5\times 10^{-5}$ to $9.0\times 10^{-4}$ m/s, column diameters from 0.0145 to 0.30 m, and column lengths from 0.0610 to 1.08 m.

In the design of the carousel process, the length of a single column segment is determined from the length of the constant-pattern mass-transfer zone at a given linear velocity. The mass-transfer zone is defined as the length of column required to contain the $Cs^+$ concentration wave from $C_b = 0.9C_f$ to $C_b = 1.3\times10^{-6}$ kg/m$^3$ after a constant-pattern wave is developed. This study shows that the estimated carousel sizes are most sensitive to the effective cesium isotherms and the intraparticle diffusivities. An analysis of the dimensionless groups in the differential mass balance equations reveals that the normalized constant-pattern mass-transfer zone length is proportional to the particle Peclet number. The proportionality constant is a function of the waste composition and the $Cs^+$ concentration. Increasing isotherm nonlinearity (higher concentration or higher Langmuir $b$ value) leads to a shorter mass-transfer zone as a result of thermodynamic sharpening effects. This trend agrees with the analytical solutions of constant-pattern waves based on a linear driving force model. The equivalent $K_f$ calculated from the results of the pore diffusion model is a function of isotherm nonlinearity. The relationships shown in Figure 11 allow one to adjust carousel designs for variations in isotherms, feed concentrations, particle size, linear velocity, and intraparticle diffusivity.

## Acknowledgment

The authors wish to thank W. Tamosaitis and C. P. McGinnis for initiating this project, S. Beck and J. Carter for providing background information, R. Jacobs for calculating $Cs^+$ isotherms from the ZAME model, D. McCabe for providing SRS simulant batch data, D. D. Lee and P. Taylor for providing and explaining MVST-W29 column data, and R. D. Hunt, K. K. Anderson, and J. L. Collins for providing the batch test data on the ''Average'' SRS waste simulant. The physical property data such as density of the ion exchanger, porosity of the packed ion-exchanger bed, pellet porosity, and initial guesses for the effective particle diffusivities provided by Drs. R. G. Anthony, M. Huckman, and I. Latheef are very much appreciated.

## Notation

$a$ = Langmuir coefficient based on solid volume, m$^3$/m$^3$ S.V.
$a_p$ = Langmuir coefficient based on particle volume, m$^3$/m$^3$ P.V. (Eq. A2)
$b$ = Langmuir coefficient, m$^3$/kg
CP-LDF = constant pattern linear driving force
CsRD = Cesium Removal Demonstration
CST = crystalline silicotitanate
$D^\infty$ = Brownian diffusivity, m$^2$/s
$F$ = volumetric flow rate, m$^3$/s
ID = column inner diameter, m
$K_d$ = distribution coefficient, $a_p/(1+bC_b)$, m$^3$/m$^3$ P.V.
$K_d^f$ = distribution coefficient of the feed concentration, m$^3$/m$^3$ P.V.
$L_c$ = column length, m
MVST-W29 = Melton Valley Storage Tank W29
$u_{sh}$ = shock-wave velocity, m/s
$V_c$ = column volume, m$^3$
ZAME model = Zheng, Anthony, Miller equilibrium model
$\epsilon_b$ = bed void fraction, dimensionless
$\epsilon_p$ = intraparticle void fraction, dimensionless

### *Dimensionless variables*

$L^* = L_c/R_p$ (dimensionless column length)
$L^*_{MTZ} = L_{MTZ}/R_p Pe_p$ (dimensionless mass-transfer zone length)
$Pe_a = u_0 R_p/E_b$ (axial Peclet number)
$Pe_p = u_0 R_p/D_p$ (particle Peclet number)
$Sh = k_f R_p/D_p$ (film mass-transfer number)
$X = zD_p/u_0 R_p^2$ (dimensionless axial position)
$Y = rD_p/u_0 R_p^2$ (dimensionless radial position)
$\tau = tD_p/R_p^2$ (dimensionless time)
$\phi_1 = C_1/C_f$ (normalized low-concentration end of mass-transfer zone)
$\phi_2 = C_2/C_f$ (normalized high-concentration end of mass-transfer zone)
$\phi_b = (1-\epsilon_b)/\epsilon_b$ (particle/bulk phase ratio)
$\phi_p = (1-\epsilon_p)/\epsilon_p$ (solid/pore phase ratio)
$\psi$ = cut factor in the constant-pattern solution (Eq. 13)

## Literature Cited

Anthony, R. G., R. G. Dosch, D. Gu, and C. V. Philip, ''Use of Silicotitanates for Removing Cesium and Strontium from Defense Waste,'' *Ind. Eng. Chem. Res.*, **33**, 2702 (1994).
Anthony, R. G., C. V. Philip, and R. G. Dosch, ''Selective Adsorption and Ion Exchange of Metal Cations and Anions with Silicotitanates and Layered Titanates,'' *Waste Manage. (N. Y.)*, **13**, 503 (1993).
Berninger, J. A., R. D. Whitley, and N.-H. L. Wang, ''A Versatile Model for Simulation of Reaction and Nonequilibrium Dynamics in Multicomponent Fixed-Bed Adsorption Processes,'' *Comp. Chem. Eng.*, **15**, 749 (1991).
Chung, S. F., and C. Y. Wen, ''Longitudinal Dispersion of Liquid Flowing Through Fixed and Fluidized Beds,'' *AIChE J.*, **14**, 749 (1968).
Ernest, Jr., M. V., J. P. Bibler, R. D. Whitley, and N.-H. L. Wang, ''Development of a Carousel Ion Exchange Process for Removal of Cesium-137 from Alkaline Nuclear Waste,'' *Ind. Eng. Chem. Res.*, **36**, 2775 (1997).
Garg, D. R., and D. M. Ruthven, ''Theoretical Prediction of Breakthrough Curves for Molecular Sieve Adsorption Columns—I. Asymptotic Solutions,'' *Chem. Eng. Sci.*, **28**, 791 (1973).
Hall, K. R., L. C. Eagleton, A. Acrivos, and T. Vermuelen, ''Pore- and Solid-Diffusion Kinetics in Fixed-Bed Adsorption under Constant-Pattern Conditions,'' *Ind. Eng. Chem. Fund.*, **5**, 212 (1966).
Huckman, M. E., I. M. Letheef, and R. G. Anthony, ''Ion Exchange of Several Radionuclides on the Hydrous Crystalline Silicotitanate, UOP IONSIV IE-911,'' *Sep. Sci. Tech.*, **34**, 1145 (1999).
Hunt, R. D., K. K. Anderson, and D. D. Lee, ''Batch Tests with IONSIV IE-911 and a Simulant of the Savannah River Site's 'Average' Supernatant: Distribution Coefficients vs. Time,'' Technical Report, Oak Ridge Nat. Lab., Oak Ridge, TN (1998).
Koh, J.-H., P. C. Wankat, and N.-H. L. Wang, ''Pore and Surface Diffusion and Bulk-Phase Mass Transfer in Packed and Fluidized Beds,'' *Ind. Eng. Chem. Res.*, **37**, 228 (1998).
Lee, D. D., J. F. Walker, Jr., P. A. Taylor, and D. W. Hendrickson, ''Cesium-Removal Flow Studies using Ion Exchange,'' *Environ. Prog.*, **16**, 251 (1997).
Ma, Z., R. D. Whitley, and N.-H. L. Wang, ''Pore and Surface Diffusion in Multicomponent Adsorption and Liquid Chromatography Systems,'' *AIChE J.*, **42**, 1244 (1996).
McCabe, D. J., ''Crystalline Silicotitanate Examination Results,'' Technical Report WSRC-RP-94-1123, Westinghouse Savannah River Co., Aiken, SC (1995).
McCabe, D. J., ''Examination of Crystalline Silicotitanate Applicability in Removal of Cesium from SRS High Level Waste,'' Technical Report WSRC-TR-97-0016, Westinghouse Savannah River Co., Aiken, SC (1997).
McGinnis, C. P., R. D. Hunt, S. M. Gibson, and R. L. Gilchrist, ''Separation Projects within the U.S. Department of Energy's Underground Storage Tank—Integrated Demonstration,'' *Sep. Sci. Tech.*, **30**, 1741 (1995).
Michaels, A. S., ''Simplified Method of Interpreting Kinetic Data in Fixed-Bed Ion Exchange,'' *Ind. Eng. Chem.*, **44**, 1922 (1952).
Ruthven, D. M., *Principles of Adsorption and Adsorption Processes*, Wiley, New York (1984).
Walker, D. D., W. D. King, D. P. Diprete, L. L. Tovo, D. T. Hobbs, and W. L. Wilmarth, ''Cesium Removal from Simulated SRS

High-Level Waste using Crystalline Silicotitanate,'' Technical Report WSRC-TR-98-00344, Westinghouse Savannah River Co., Aiken, SC (1998a).
Walker, Jr., J. F., P. A. Taylor, R. L. Cummins, B. S. Evans, S. D. Heath, J. D. Hewitt, R. D. Hunt, H. L. Jennings, J. A. Kilby, D. D. Lee, S. Lewis-Lambert, S. A. Richardson, and R. F. Utrera, ''Cesium Removal Demonstration Utilizing Crystalline Silicotitanate Sorbent for Processing Melton Valley Storage Tank Supernate: Final Report,'' Technical Report ORNL/TM-13503, Oak Ridge Nat. Lab., Oak Ridge, TN (1998b).
Wankat, P. C., *Rate-Controlled Separation*, Chapman & Hall, New York (1994).
Whitley, R. D., ''Dynamics of Nonlinear Multicomponent Chromatography—Interplay of Mass Transfer, Intrinsic Sorption Kinetics, and Reaction,'' PhD Diss., Purdue Univ., West Lafayette, IN (1990).
Whitley, R. D., K. E. Van Cott, and N.-H. L. Wang, ''Analysis of Nonequilibrium Adsorption/Desorption Kinetics and Implications for Analytical and Preparative Chromatography,'' *Ind. Eng. Chem. Res.*, **32**, 149 (1993).
Wilson, E. J., and C. J. Geankoplis, ''Liquid Mass Transfer at Very Low Reynolds Numbers in Packed Beds,'' *Ind. Eng. Chem. Fundam.*, **5**, 9 (1966).
Zheng, Z., R. G. Anthony, and J. E. Miller, ''Modeling Multicomponent Ion Exchange Equilibrium Utilizing Hydrous Crystalline Silicotitanates by a Multiple Interactive Ion Exchange Site Model,'' *Ind. Eng. Chem. Res.*, **36**, 2427 (1997).

## Appendix: Constant-Pattern Solution for the Linear Driving Force Model and Definition of Parameters

If it is assumed that the shockwave velocity is constant and equal to the velocity of the feed concentration, then one may write (Wankat, 1994)

$$\frac{Q_p}{C_b} = \frac{Q_{p,f}}{C_f} = \frac{a_p}{1+bC_f} \tag{A1}$$

where $Q_p$ represents the particle-phase concentration (kg/m$^3$ P.V.) and $Q_{p,f}$ represents the particle-phase concentration in equilibrium with the feed concentration $C_f$ (kg/m$^3$). $Q_p$ differs from the variable $Q$ in Eqs. 1 to 4 in that $Q_p$ considers the solute concentration in the pore and solid phases, whereas $Q$ takes into account only the solute that is in the solid phase. $Q_p$ is a function of $C_b$; $Q$ is a function of $C_p$. The value of $a_p$ is therefore defined in terms of the particle volume, which is different from the value of $a$ reported previously in this work

$$a_p = \epsilon_p(1+bC_f) + (1-\epsilon_p)\,a \tag{A2}$$

Integrating Eq. 8 between $C_1 = \phi_1 C_f$ and $C_2 = \phi_2 C_f$ yields an expression for the difference in time between the high- and low-concentration ends of the mass-transfer zone with respect to a stationary observer for an initially clean column

$$\Delta t = \frac{1}{K_f}\frac{a_p}{1+bC_f}\left[\frac{1}{bC_f}\ln\left(\frac{\phi_2(1-\phi_1)}{\phi_1(1-\phi_2)}\right)+\ln\left(\frac{\phi_2}{\phi_1}\right)\right] \tag{A3}$$

The constant-pattern wave travels at the shockwave velocity of the feed concentration, which is given by the following equation

$$u_{sh} = \frac{u_0}{1+\dfrac{1-\epsilon_b}{\epsilon_b}\dfrac{\Delta Q_p}{\Delta C_b}} \tag{A4}$$

where

$$\frac{\Delta Q_p}{\Delta C_b} = \frac{a_p}{1+bC_f} \tag{A5}$$

for an initially clean column subjected to a step-change to $C_f$. Since $L_{\mathrm{MTZ}} = u_{sh}\Delta t$, combining Eqs. A3 and A4 yields the length of the mass-transfer zone

$$L_{\mathrm{MTZ}} = \frac{u_0}{1+\dfrac{1-\epsilon_b}{\epsilon_b}\dfrac{a_p}{1+bC_f}}\left(\frac{1}{K_f}\right)\left(\frac{a_p}{1+bC_f}\right) \times\left[\frac{1}{bC_f}\ln\left(\frac{\phi_2(1-\phi_1)}{\phi_1(1-\phi_2)}\right)+\ln\left(\frac{\phi_2}{\phi_1}\right)\right] \tag{A6}$$

The analytical solutions to the linear driving force model can be recast as dimensionless groups by multiplying both sides of Eq. A6 by $D_p/u_0 R_p^2$

$$\frac{L_{\mathrm{MTZ}}}{R_p Pe_p} = \left(\frac{D_p}{R_p^2 K_f}\right)\frac{1}{1+\dfrac{1-\epsilon_b}{\epsilon_b}\dfrac{a_p}{1+bC_f}}\left(\frac{a_p}{1+bC_f}\right) \times\left[\frac{1}{bC_f}\ln\left(\frac{\phi_2(1-\phi_1)}{\phi_1(1-\phi_2)}\right)+\ln\left(\frac{\phi_2}{\phi_1}\right)\right] \tag{A7}$$

If one defines the following dimensionless variables

$$\frac{u_{sh}}{u_0} = \frac{1}{1+\dfrac{1-\epsilon_b}{\epsilon_b}\dfrac{a_p}{1+bC_f}} \tag{A8}$$

$$\psi = \left(\frac{a_p}{1+bC_f}\right)\left[\frac{1}{bC_f}\ln\left(\frac{\phi_2(1-\phi_1)}{\phi_1(1-\phi_2)}\right)+\ln\left(\frac{\phi_2}{\phi_1}\right)\right] \tag{A9}$$

then it is clear that a plot of $L_{\mathrm{MTZ}}/R_p Pe_p$ vs. $\psi u_{sh}/u_0$ should yield a straight line with a slope of $D_p/R_p^2 K_f$.

*Manuscript received Dec. 28, 1998, and revision received Nov. 5, 1999.*